Title: The number of cytokinesis nodes in mitotic fission yeast scales with cell volume

Wasim A. Sayyad[1] and Thomas D. Pollard[1,2, 3,*]

[1]Department of Molecular Cellular and Developmental Biology

[2]Department of Molecular Biophysics and Biochemistry

[3]Department of Cell Biology

Yale University, PO Box 208103

New Haven, CT 06520-8103 USA

*Correspondence: thomas.pollard@yale.edu

Abstract

Cytokinesis nodes are assemblies of stoichiometric ratios of proteins associated with the plasma membrane, which serve as precursors for the contractile ring during cytokinesis by fission yeast. The total number of nodes is uncertain, because of the limitations of the methods used previously. Here we used the ~140 nm resolution of Airyscan confocal microscopy to resolve a large population of dim, unitary cytokinesis nodes in 3D reconstructions of whole fission yeast cells. Wild-type fission yeast cells make about 200 unitary cytokinesis nodes. Most, but not all of these nodes condense into a contractile ring. The number of cytokinesis nodes scales with cell size in four strains tested, although wide *rga4Δ* mutant cells form somewhat fewer cytokinesis nodes than expected from the overall trend. The surface density of Pom1 kinase on the plasma membrane around the equators of cells is similar with a wide range of node numbers, so Pom1 does not control cytokinesis node number. However, varying protein concentrations with the *nmt1* promoter showed that the numbers of nodes increase above a baseline of about 200 with the total cellular concentration of either Pom1 or the kinase Cdr2.

Introduction

Cytokinesis nodes are stoichiometric assemblies of multiple proteins, which associate with the plasma membrane around the middle of fission yeast cells and polymerize actin filaments that form the cytokinetic contractile ring (Vavylonis et al., 2008). Similar assemblies containing myosin-II may form contractile rings in other cells (Beach et al., 2014; Henson et al., 2017; Hickson & O'Farrell, 2008; Werner et al., 2007). In fission yeast, cytokinesis nodes form from two distinct types of interphase nodes (Akamatsu et al., 2014). At the end of cytokinesis, type 1 nodes containing kinases Cdr1 and Cdr2 appear in a broad band around the middle of the cell as SIN activity drops (Pu et al., 2015) and remain stationary throughout interphase (Akamatsu et al., 2014; Martin & Berthelot-Grosjean, 2009; Morrell et al., 2004; Moseley et al., 2009). Type 2 nodes containing the proteins Blt1p, Klp8p, Gef2p, and Nod1p (Jourdain et al., 2013; Martin & Berthelot-Grosjean, 2009; Morrell et al., 2004; Moseley et al., 2009; Ye et al., 2012) originate from the constricting contractile ring from the previous cell cycle and diffuse along the plasma membrane. During the G_2 phase of the cell cycle, type 1 nodes capture diffusing type 2 nodes to form cytokinesis nodes (Akamatsu et al., 2014). During ten minutes prior to spindle pole body (SPB) separation, cytokinesis nodes mature by sequentially accumulating stoichiometric ratios of

myosin-II (Myo2 heavy chain and two light chains), IQGAP Rng2p and F-BAR Cdc15p (Vavylonis et al. 2008, Wu et al 2006). At the time of SPB separation, smaller numbers of formin Cdc12p join each node, where they nucleate and elongate actin filaments (Wu et al., 2006; Laporte et al., 2011). Interactions between actin filaments from one node and myosin in adjacent nodes pull the nodes together into a contractile ring (Vavylonis et al. 2008). Interestingly, 10-12 min after SPB separation the Cdr2p-mEGFP disperses from the newly-formed contractile ring into the cytoplasm due to high SIN activity (Akamatsu et al., 2014; Martin & Berthelot-Grosjean, 2009; Morrell et al., 2004; Moseley et al., 2009).

The rod-shaped fission yeast cells grow linearly at the cell tips and maintain a constant width (Fantes & Nurse, 1977; Moreno et al., 1989). Before division, cells reach a threshold size with double the initial cell length (Gu & Oliferenko, 2019; Neumann & Nurse, 2007). During this period, the interphase nodes also double in number (Allard et al., 2018; Pan et al., 2014). Interphase nodes are important to sense the surface area of the cell rather than its length or volume to control cell size at the time of division (Facchetti, Knapp, Chang, et al., 2019; Pan et al., 2014).

Before entering mitosis, interphase nodes mature into cytokinesis nodes. Accurate measurements of node numbers are important for two reasons. First, the number of nodes is a key parameter in models and computer simulations to test ideas about the mechanisms of contractile ring assembly and constriction. Second, estimates of the number of molecules per node have generally relied on measuring the total numbers of each protein in the broad band of nodes and then dividing by the number of nodes (Laplante, Huang, et al., 2016; Vavylonis et al., 2008).

Nevertheless, measuring the number of cytokinesis nodes in fission yeast cells has been challenging. Vavylonis et al (2008) counted 63 ±10 cytokinesis nodes tagged with Rlc1p-3GFP in the broad bands of wild-type cells in 3D reconstructions of z-series acquired by spinning disk confocal microscopy. Nodes varied considerably in intensity; nodes with low intensities grouped in one main peak; a higher intensity peak was attributed to pairs of unresolved nodes, and additional nodes had even higher intensities. Interphase nodes marked with Cdr2, Cdr1, Mid1, Blt1, Gef2, or Klp8 had a wide range of intensities (Moseley et al. 2009) and included well separated, dim nodes with the fluorescence included entirely in five z-sections and in regions 7

pixels in diameter (Akamatsu et al., 2017). Deng et al. (2013) applied deconvolution to images obtained in wide-field microscopy and counted ~52–106 interphase nodes tagged with Cdr2-mCherry. Pan et al. (2014) used the Find Maxima macro function in ImageJ to find pixels with maximum intensity in maximum projection images and counted <50 interphase nodes and noted that the number scaled with cell length. However, they ignored dim nodes by choosing the only pixels in ROI with intensities greater than approximately twice the mean background intensity. Using the same scaled fire LUT plugin in ImageJ Willet et al. (2019) measured ≤ 15 nodes marked with Mid1 in wild-type cells that had a yellow, orange, or white intensity but did not count dim purple or red intensity nodes (Willet et al., 2019).

Akamatsu et al. (2017) showed that the total cell concentrations of Cdr2, Cdr1, Mid1, Blt1, Gef2, and Klp8 are constant across the cell cycle, so the numbers of these proteins increase as the cell grows. The intensities of type 1 node proteins Cdr2, Cdr1, and Mid1 in the broad band increased linearly over time during G_2, so either the number of type 1 nodes or their protein content increases over time. The intensity of the type 2 node marker Blt1 increases in the broad band as the type 2 nodes capture diffusing type 1 nodes. These interphase nodes vary considerably in intensity. Small, dim nodes predominate, and more intense nodes have multiples of the intensity of these 'unitary nodes'.

Akamatsu et al. (2017) and Laplante et al. (2018) employed single-molecule localization super-resolution microscopy (SMLM) to overcome the resolution limit of confocal microscopy. The 35 nm resolution of this method revealed that interphase and cytokinesis nodes are much smaller (<100 nm) than their diffraction-limited images in confocal micrographs. Some nodes were so close together that they had twice or three times the numbers of localizations of unitary nodes. Laplante et al. (2018) used two methods to estimate the number of cytokinesis nodes in fission yeast broad bands. One was to measure the local density of nodes in a 400 nm optical section from the top or bottom of the cell and then to extrapolate this density around the equator, giving ~140 total nodes for five different tagged proteins (Mid1, Rlc1, Cdc15, Myo2, and Rng2). The second method was to blur the SMLM images with the point spread function to simulate a confocal image. This resulted in about half the unitary nodes being blurred together, so the 65 nodes counted by Vavylonis et al. (2008) represented about 130 unitary nodes.

Allard et al. (2018) used the superior (140 nm) resolution of Airyscan microscopy and an automated particle tracking plugin to count ~50 nodes tagged with Cdr2-mEGFP. However, the algorithm used in the plugin was designed to find only local intensity maxima and did not count the dim nodes with low intensities.

We used Airyscan microscopy to image mitotic fission yeast cells tagged with the type 2 node protein Blt1 and determined the numbers of cytokinesis nodes in wild-type cells as well as strains with a wide range of sizes. The improved resolution allowed us to detect more dim cytokinesis nodes than resolved by conventional confocal microscopy. The resolution of SMLM is four-fold better than Airyscan, but Airyscan allows 3D reconstructions of a whole, live cells, enabling us to compare the intensities of Blt1-mEGFP in dim unitary nodes to the total intensity of Blt1-mEGFP in the broad band of the same cell. These two measurements allow one to calculate directly the number of cytokinesis nodes around the equator from the ratio of total intensity to unitary node intensity. Wild-type fission yeast cells have about 200 cytokinesis nodes in the broad band that condenses into a contractile ring incorporating three-fourths of the cytokinesis nodes. Most importantly, the number of cytokinesis nodes scales directly with cell volume in strains that are smaller or larger than wild-type cells. Pom1 controls the width of the broad band of nodes and Cdr2 partly controls the number of nodes.

Results

We marked nodes in mitotic cells with Blt1p-mEGFP. Blt1 is a scaffold protein for type 2 nodes and is the only protein known to persist in nodes throughout the cell cycle, so it is found in interphase nodes, cytokinesis nodes, and contractile rings (Coffman et al., 2009; Ye et al., 2012). We marked SPBs with Sad1-RFP to identify mitotic cells. Mitotic cells have two SPBs, so we selected cells with two closely-spaced SPBs to image and measure cytokinesis nodes in prophase/metaphase cells. The fluorescent proteins were integrated into the haploid genome to ensure that all copies of each protein were tagged and expressed at normal levels.

Airyscan fluorescence microscopy resolves dim unitary cytokinesis nodes in a broad band

We used a Zeiss Airyscan fluorescence microscope to acquire 40 Z-slices covering the entire volume of cells to measure the total and local fluorescence of Blt1-mEGFP in wild-type fission yeast cells in 2-3 s. The frame size and pixel dwell time were adjusted so that motions of cytokinesis nodes (20 nm/s; (Vavylonis et al., 2008)) did not blur the images during image

acquisition. Cytokinesis nodes appeared as a broad band of fluorescence spots in the cortex around the middle of mitotic cells with two SPBs. The fluorescence intensities of these spots ranged from very bright to dim (Figure 1 A, upper panel).

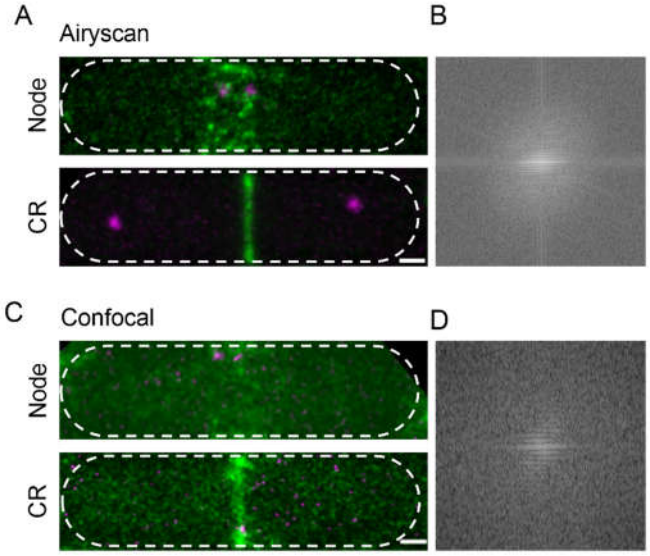

Figure 1. Comparison of Airyscan and confocal images of cytokinesis nodes and contractile rings in wild-type fission yeast cells expressing Blt1-mEGFP (green) and Sad1-RFP showing two spindle pole bodies (magenta). (A) Airyscan images. Max projections of 40 Z- slices. The upper cell has a broad band of cytokinesis nodes (green). The lower cell has a contractile ring. (B) Fast Fourier transform of the image in lower panel A, green channel. (C) Confocal images. Max projections of 20 Z-slices of confocal fluorescence with 0.6 AU+8X averaging1 + iteratively constrained deconvolution micrographs. The upper cell has broad band of cytokinesis nodes. The lower cell has a contractile ring. (D) Fast Fourier transform of the image in lower panel C, green channel). The scale bar is 1 µm.

To compare the high resolution and sensitivity of Airyscan to a conventional laser scanning confocal microscope, we used the same Airyscan detector in confocal mode with a pinhole of 0.6 AU, 8X line averaging + linear constrained iterative deconvolution, and 2X laser intensity to compensate for the lower signal to noise ratio. Large nodes stood out in the confocal images, but the higher background noise made it difficult to detect the dim cytokinesis nodes in broad bands. Contractile rings were brighter and narrower in Airyscan than confocal images (Figure 1 A and C, lower panels). Fast Fourier transform analysis of images of cells with contractile rings showed that Airyscan retrieved higher frequencies and more extensively distributed information. The horizontal line in the frequency domain of the Airyscan image corresponds to the contractile ring (Figure 1B), which was absent in the frequency domain of the confocal image (Figure 1D). This shows that with 3D reconstruction ability similar to confocal microscopy, Airyscan imaging can resolve small, dim unitary cytokinesis nodes. We interpret the

dim nodes as unitary nodes, while the brighter nodes consist of two or more unitary nodes (Akamatsu et al., 2017; Laplante, Huang, et al., 2016) located too closely to be resolved.

Time-lapse imaging showed that cytokinesis nodes of all sizes, including unitary nodes, condensed into bigger and brighter nodes as they coalesce into a contractile ring during 10-12 min after separation of the SPBs as described for the brighter fraction of the population of nodes by confocal microscopy (Vavylonis et al., 2008). Neither the Airyscan nor confocal microscopy resolved cytokinesis nodes known to be present in contractile rings (Figure 1A and C, lower panels) by single-molecule localization microscopy (Laplante, Huang, et al., 2016).

Counting cytokinesis nodes in the broad band and contractile ring

The methods section explains how we used the three-dimensional distribution of fluorescence of spots around the equator to identify nodes (Figure 2A) and measure their fluorescence. To qualify as a node, the fluorescence had to be confined in the X-Y plane within a circle 12-pixels (0.5 μm) in diameter and in the Z direction to 7 z-slices of 170 nm (1.1 μm). The total fluorescence within the 12-pixel diameter circle in 7 z-slice images was sum projected and measured as a node fluorescence (Figure 2B). From the same sum projected image we calculated the average fluorescence from 8 equivalent volumes of cytoplasm near each cell tip where nodes were absent (Figure 2B). The fluorescence of each candidate node was its total fluorescence minus the average cytoplasm fluorescence.

We measured the fluorescence of 280 unitary nodes in 24 mitotic, wild-type cells and plotted a histogram to determine the distribution of intensities and the average fluorescence intensity (Figure 2D). The fluorescence intensities of dim cytokinesis nodes formed a broad, normal distribution with the mean value of 2454 AU and a standard deviation of 1074 AU. The 2% of nodes with fluorescence ~5000 AU are likely unresolved binary nodes.

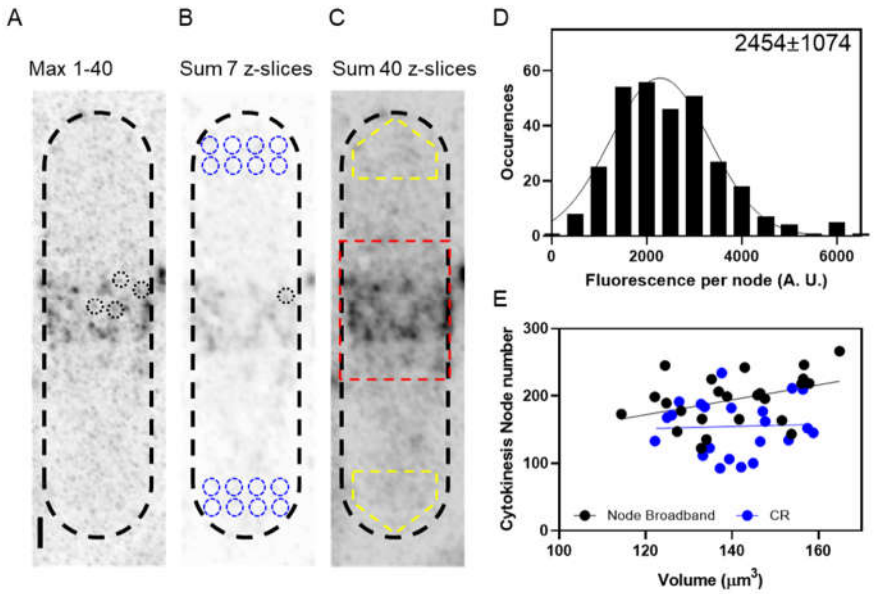

Figure 2. Counting cytokinesis nodes in broad bands and contractile rings of wild-type cells expressing Blt1-mEGFP. (A) Reverse contrast fluorescence micrograph of Figure 1A upper panel. Black dotted circles are dim nodes selected for fluorescence measurements. (B) Reverse contrast fluorescence micrograph of a sum projection of seven slices of the cell in panel A. Black dotted circles mark spots selected to measure the fluorescence of unitary nodes and blue dotted circles mark cytoplasmic regions selected to measure background fluorescence. (C) Reverse contrast fluorescence micrograph of a sum projection of 40 Z-slices of the cell in panel A. The red rectangle outlines the region used to measure the total node broad band intensity and the yellow polygonal area marks the area chosen to measure background intensity to subtract from the broad band area. (D) Histogram of the distribution of fluorescence intensities of a sample of 280 dim cytokinesis nodes presumed to be unitary nodes from 24 cells. The continuous curve is a fit of a Gaussian distribution to the data with the mean value of 2454 and standard deviation of 1074. (E) The total number of unitary Blt1-mEGFP nodes in broad bands (Black points, 24 cells) and contractile rings (Blue points, 22 cells) as a function of cell volume. These numbers are the ratios of the background-corrected total fluorescence in broad bands of nodes or contractile rings to the mean fluorescence of a unitary node. The slopes of the corresponding linear regressions are not significantly different from zero ($p = 0.06$, for node broadband, and $p = 0.8$ for contractile rings).

We estimated the number of unitary nodes in broad bands of wild-type fission yeast cells from the ratio of total intensity (corrected for cytoplasmic background) of Blt1-mEGFP in a broad band around the equator of a given cell to the intensity of Blt1-mEGFP in an average unitary node, 2400±1000 AU (Figure 2D). We used 3D reconstructions of stacks of Airyscan images to measure the total fluorescence of all the cytokinesis nodes around the equator of each cell for direct comparison with the average fluorescence of unitary nodes.

D'Agostino-Pearson's normality test showed that the values of these ratios of total broad band fluorescence to the fluorescence of a unitary node were distributed normally ($p = 0.8$) with a mean of 200 and SD of 40 nodes per cell (Figure 2E). This number is more than three-fold that

reported by Vavylonis et al (2008) from spinning disk confocal images where only bright cytokinesis nodes were resolved.

We measured the total Blt1-mEGFP fluorescence of contractile rings of wild-type cells and after cytoplasmic background subtraction divided these totals by the average unitary node fluorescence to estimate the total numbers of unitary nodes (Figure 2E). This ratio was 154, somewhat lower than the total node number in broad bands. We conclude that wild-type fission yeast cells have on average 200 cytokinesis nodes, most of which are incorporated into the contractile ring.

Mutant strains with a range of cell volumes

Wild-type fission yeast cells undergo mitosis when they reach lengths of 12-15 μm, but their actual volumes vary from about 110 μm^3 to 170 μm^3. Within this naturally occurring variation in sizes, the number of unitary nodes in the broad band tended to increase with cell volume (Figure 2E). This observation motivated us to count the numbers of nodes in mitotic cells with a range of sizes. We used 5 different mutant strains, described in the following paragraphs, and hydroxyurea to create cells that varied in volume from 24 μm^3 to 450 μm^3 (Figure 3).

The Wee1 kinase catalyzes the phosphorylation of Cdc2/Cdk1 to prevent cells from entering mitosis (Russell & Nurse, 1987). At the restrictive temperature of 36°C, *wee1-50* cells enter mitosis prematurely, so they are smaller than normal (Paul Nurse, 1975). After 4 h at the restrictive temperature, the average cell length of *wee1-50* mutant cells (7.8 ±1 μm) was about half the average length of wild-type cells (14 ± 1 μm) (Figure 3C). The diameter of *wee1-50* mutant cells (3.7 ±0.2 μm) was the same as wild-type cells (3.7 ±0.1 μm). When released to the permissive temperature, most cells started to form a contractile ring in 10-15 min. The broad band of nodes looked more dispersed in these cells than in other strains.

The Cdc25 phosphatase removes the inhibitory phosphates added by Wee1 from Cdc2/Cdk1 to allow cells to enter mitosis (P Nurse, 1990; Russell & Nurse, 1986, 1987). At the restrictive temperature of 36°C, *cdc25-22* mutant cells arrest at the G_2/M transition but continue growing at both ends. We varied the time at 36°C to obtain a range of lengths. After 4-6 h at 36°C cells were 26.9 ±5.8 μm long, twice the average of wild-type cells but did not differ significantly in diameter (3.9 ±0.1 μm) (Figure 3A). The *cdc25-22* mutant cells produced a wide range of cell sizes, so we grouped them by size. When released to the permissive temperature,

most of the cells synchronously entered mitosis within 1 h and formed a broad band of cytokinesis nodes.

The RhoGAP Rga4 localizes to the division site of cells and inactivates the GTPase Cdc42 (Das et al., 2007). Cells with deletion mutations of *rga4* are shorter (11.6 ± 1.0 μm) but have larger diameters (4.4 ±0.2 μm) than wild-type cells (Das et al., 2007; Tatebe et al., 2008) (Figure 3D). Treating *rga4Δ* cells with 15 mM hydroxyurea for 4-6 h inhibited DNA synthesis by inactivating ribonucleoside reductase (Krakoff et al., 1968) and arrested the cells in the S phase during which they grew longer (J.M.MitchisonJ.Creanor, 1971) (Figure 3F). On the other hand, RhoGAP Rga2 localizes to growing cell tips and inactivates the Rho2 GTPase (Villar-Tajadura et al., 2008). Deletion of *rga2* does not change the cell length but decreases the cell diameter (3.4 ±0.2 μm) (Villar-Tajadura et al., 2008) (Figure 3E).

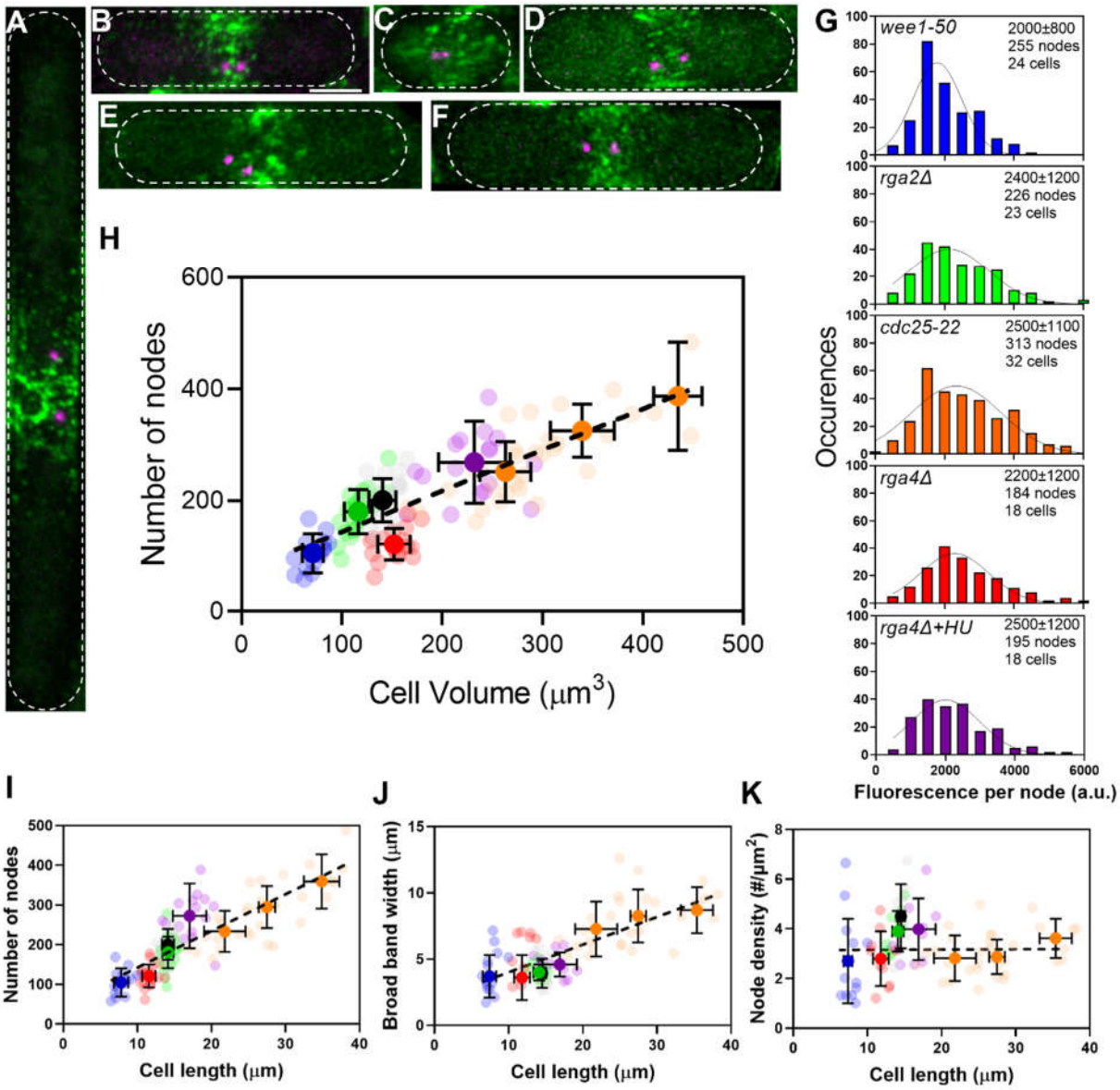

Figure 3. The number of cytokinesis nodes scales with the size of the cell. (A-F). Maximum intensity projections of Airyscan images 40 Z-sections of fission yeast cells expressing Blt1-mEGFP and Sad1-RFP showing two spindle pole bodies (magenta). The scale bar is 3 µm. (A) *cdc25-22*; (B) wild type; (C) *wee1-50*; (D) r*ga4Δ*; (E) *rga2Δ*; and (F) *rga4Δ*+HU at 25°C. (G) Histograms of the distributions of fluorescence intensities of dim nodes in five different strains. Wild type is also shown in Fig. 2C. Insets show average unitary node fluorescence intensity ± S.D for each strain. Tukey's multiple comparison test showed that *wee1-50* differs significantly from the other strains with p <0.005. (H-K) Relationships between node parameters (numbers, broad band width and densities) and cell size parameters in five strains: *wee1-50* (n = 16); *rga2Δ* at (n = 23); wild type at (n = 24); r*ga4Δ* at (n = 17); and *rga4Δ*+HU (n = 17) at 25°C. All measurements for each strain are collected in one bin except for *cdc25-22* cells, which are divided into three volume bins: 200-300 µm^3, n = 18; 300-400 µm^3, n = 13; >400 µm^3, n = 4 and three length bins: 15-25 µm, n = 14; 25-30 µm, n = 10; 30-40 µm, n = 7. The transparent symbols are measurements of individual cells. The solid symbols are the mean numbers of node parameters. Except for the *cdc25-22* cells, the vertical error bars show the SD of the mean numbers and horizontal error bars the SD of the lengths. For the *cdc25-22* (volume > 400 µm^3) cells the error bar is the range. The dotted black lines are linear regressions using all the data points. (H) Node number vs. cell volume. The slope of the linear regression (black dotted line) is significantly

nonzero ($P < 0.0001$; $R^2 = 0.6$). (I) Node number vs. cell length. The slope of the linear regression (black dotted line) is significantly nonzero ($P < 0.0001$; $R^2 = 0.6$). (J) Width of node broad band as a function of cell length. The slope of the linear regression (black dotted line) is significantly nonzero ($P < 0.0001$; $R^2 = 0.5$) (K) Node density on the cortex of the broadband area as a function of cell length. The slope of the linear regression (black dotted line) is significantly zero ($P = 0.9$; $R^2 = 0.00005$). n is the number of cells.

Numbers of unitary nodes scale with cell volume

We measured the numbers of cytokinesis nodes in the mutant strains by dividing the total Blt1 fluorescence around the equator of each cell by the average intensity of the unitary nodes in that strain (Figure 2). The distributions of intensities Blt1 fluorescence of dim cytokinesis nodes were similar (around 2500 AU) in wild-type cells (Figure. 2C) and three of the experimental strains (Figure. 3G). The *wee1-50* mutant cells were an exception with an average node intensity of 2000±800, 80% of the others (Figure 3K). The broad band of cytokinesis nodes around the middle of the cells was less distinct in the *wee1-50* mutant strain (Figure. 3A-F).

The numbers of cytokinesis nodes in our sample of 129 cells were strongly correlated with cell volume (Figure 3H) with a slope of about 1 node per μm^3 of volume. This line does not extrapolate to the origin. Plotting the same data on node numbers vs. cell length (Figure. 3I) showed the same linear relationship seen for cell volume.

Comparing the numbers of cytokinesis nodes in wild-type cells, *rga4Δ* cells, and *rga2Δ* cells provided data on the effect of cell diameter on the number of cytokinesis nodes. The number of cytokinesis nodes in long, narrow *rga2Δ* cells (180 ±40) was indistinguishable from wild-type cells (200 ±40) and aligned with the data from the other strains in plots of node number vs. length and volume. On the other hand, the short, wide *rga4Δ* cells had fewer cytokinesis nodes (116 ±30) than the wild-type and *rga2Δ* mutant cells with similar volumes (Figure 3H). The *rga4Δ* cells grew longer in 15 mM hydroxyurea for 4-6 h and had the same number of nodes per volume as the other strains (Figure 3H).

The density of nodes in the broad band (Figure 3K) did not vary with cell size, so a total number of nodes increased with cell size by expanding the width of the broad band (Figure 3J). We measured the width of the broad band of cytokinesis nodes as the zone where the Blt1-mEGFP signal was >20% of the peak intensity. We calculated the density of nodes in broad bands taking into account the cell diameters, which were the same in wild-type, *wee1-50*, and *cdc25-22* mutant cells but larger in *rga4Δ* cells and smaller in *rga2Δ* cells.

Does Pom1 control the number of nodes?

We performed two types of experiments to investigate the relationship between the membrane-bound Pom1 kinase and the number of cytokinesis nodes. Concentrating Pom1 at the poles depends on microtubules that transport the polarity proteins Tea1 and Wsh3/Tea4 to the poles (Bähler & Pringle, 1998; Martin & Berthelot-Grosjean, 2009; Moseley et al., 2009; Tatebe et al., 2005). First, we measured the distributions of Pom1 in cells with a wide range of sizes by time-lapse, spinning disk confocal microscopy (Figure. 4). The five strains were wild-type, *rga4Δ*, *rga2Δ*, *cdc25-22,* and *wee1-50*. The cells expressed Pom1-GFP along with Sad1-RFP to identify mitotic cells with two SPBs and Blt1-mCherry to track nodes. Second, we varied the concentration of Pom1 and measured the number of nodes (Figure 5).

Figure 4A shows time series of fluorescence micrographs of individual cells from three strains paired with scans of the fluorescent intensity of Pom1-GFP along the lengths of these cells, while Figure 4B shows the average distributions of Blt1mCherry plus Sad1-RFP (magenta) and Pom1-GFP (green) along the lengths of 7-9 mitotic cells of the five different strains. To our knowledge, this is the first time that the distribution of Pom1 was documented in cells with such a wide range of sizes (lengths of 8 to 40 μm).

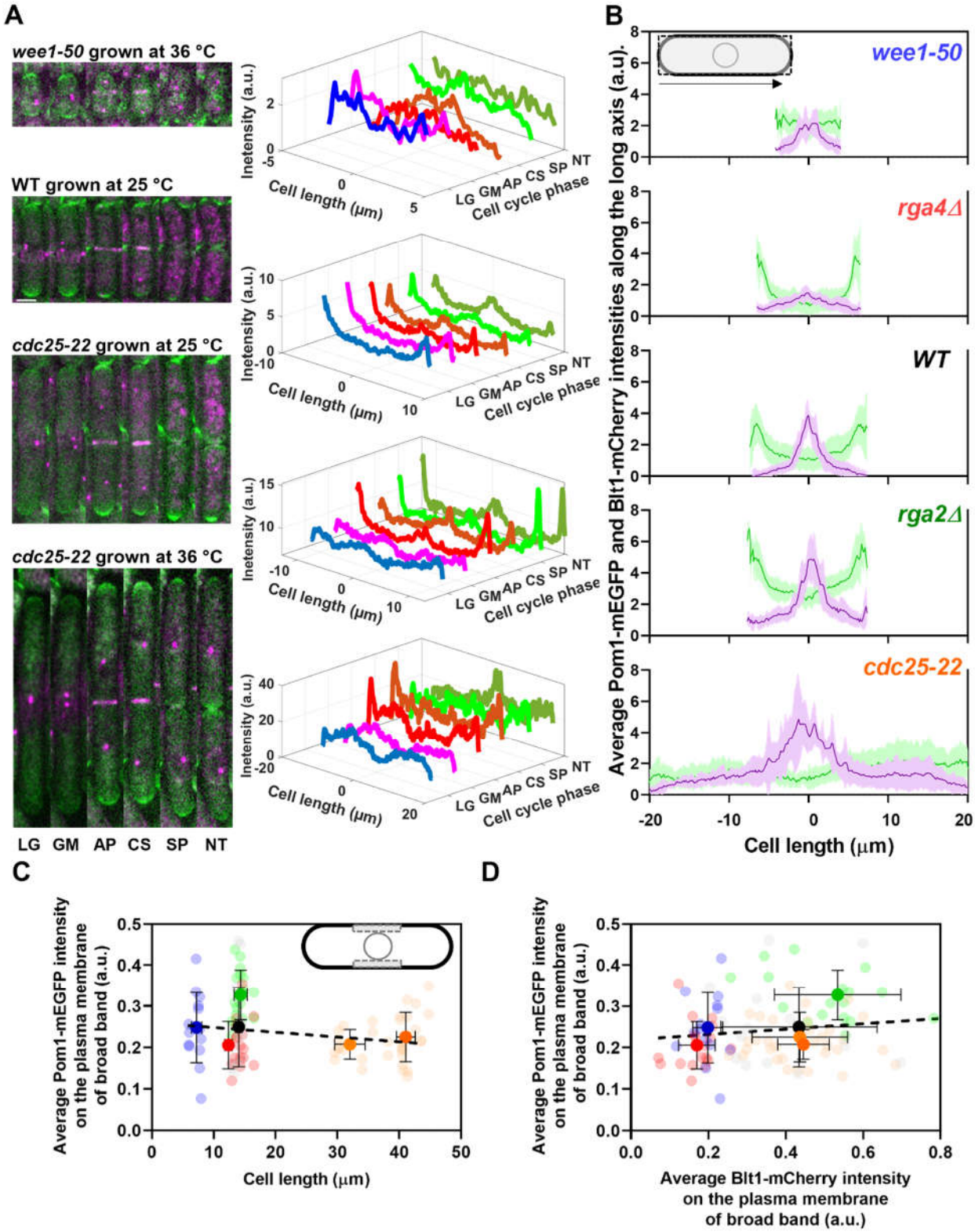

Figure 4. Distributions of Pom1 and Blt1 in cells that differ in size. (A) Distribution of Pom1 in wild type, *wee1-50,* and *cdc25-22* mutant cells. Each strain expressed Pom1-GFP and Blt1-mCherry-Sad1RFP from their native loci. Each panel has two parts: (left) sum projected confocal images of 15 Z slices of wild-type cells taken at different

phases of life cycle abbreviated as LG (late G_2), GM (G_2/M), AP (anaphase), CS (constriction), SP (separation) and NT (new end take off); and (right) time series of plots of the average intensity of Pom1-GFP fluorescence along the length of the cells. Scale bar 3 µm. (Top panel) *wee1-50* grown at 36ºC and imaged at 22ºC. (Second panel) Wild-type cells were grown at 25ºC and imaged at 22ºC. (Third panel) *cdc25-22* mutant cells grown at 25ºC and imaged at 22ºC. (Bottom panel) *cdc25-22* mutant cells grown at 36ºC for 4 h before imaging at 22ºC. (B) Distributions of Pom1 and Blt1 in cells at the G_2/M transition measured by confocal microscopy of wild-type and four mutant strains. Cells were grown at 25°C and imaged at 22°C: (●, n = 9) WT, (●, n = 7) *wee1-50*, (●, n = 8) *cdc25-22*, (●, n = 9) *rga2Δ* and (●, n = 9) *rga4Δ* mutant cells. Continuous lines are average fluorescence intensities of Blt1-mCherry-Sad1-RFP (magenta) and Pom1-GFP (green) across the full width of the cells and along the lengths of the cells. Light vertical bars are SD's. (C) Average Pom1-mEGFP intensity per pixel along the plasma membrane across the broad band of nodes in the middle focal plane of the cells as a function of the lengths of the cells. The inset shows the rectangle three pixels wide and the length of the broad band of nodes used to make the measurements. The slope of the linear regression (black dotted line) is significantly zero ($P = 0.07$; $R^2 = 0.03$). (D) Graph of the average Pom1 -mEGFP intensity per pixel vs the average Blt1-mCherry intensity per pixel along the plasma membrane in the middle focal plane of the cells (as in the inset of panel C). The slope of the linear regression (black dotted line) is significantly zero ($P = 0.13$; $R^2 = 0.02$).

Wild-type cells imaged at 22°C concentrated Pom1 at the cell tips throughout interphase and then at the division site in anaphase (Figure 4A, second panel from top) as reported previously (Bähler & Pringle, 1998). Time-lapse imaging showed that Pom1 followed the constricting contractile ring and disappeared from the division site after the cells separated. Consequently, after cell division, the concentration of Pom1 was higher at the old cell ends than at the new ends. As the growth of the new ends took off, Pom1 concentrated at the new ends with gradients toward the middles of the cells.

The behavior of Pom1 in the very short *wee1-50* cells grown at 36° C for 4 h and imaged at 22° C was mostly similar to wild-type cells. However, when cells formed a contractile ring, the Pom1 decreased at cell tips as it distributed more homogeneously along the length of the cells. Then it concentrated at the division site and followed the constricting contractile ring as seen in wild-type cells (Figure 4A, upper panel).

The behavior of Pom1 was similar in wild-type, *rga2Δ,* and *rga4*Δ cells grown at 25°C. During interphase, the Pom1-GFP intensity was highest at the tips and low in the middle of the cells. This was exaggerated in the *rga4*Δ cells (Figure 4B, second panel from top). Pom1-GFP accumulated at the division site and followed the cleavage furrow as the cells divided.

During interphase at the nonrestrictive temperature Pom1 concentrated at the cell tips of *cdc25-22* mutant cells as in other strains (Figure 4A, third panel). However, at G_2/M transition the Pom1 concentration decreased at both cell tips, and the fluorescence redistributed

homogeneously in the cytoplasm. Similarly, when *cdc25-22* cells were grown at a restrictive temperature of 36°C for 4 h and released at the imaging temperature of 22°C to synchronize them at the G_2/M boundary, Pom1 was initially distributed throughout the cytoplasm (Figure 4A, fourth panel). Then Pom1 accumulated at both cell tips peaking during anaphase when the contractile ring formed and matured. Similar to wild-type cells, Pom1 concentrated at the cleavage site and appeared to follow the constricting contractile ring (CS) until it redistributed from the division site to the new ends of daughter cells as they took off and grew (Figure 4A, third and fourth panels).

The local intensities of Pom1-mEGFP along the plasma membrane in the broad band did not vary significantly in the five strains with a five-fold range of sizes (Figure 4C) and 100-400 nodes (Figure 3H). The local Pom1 concentration did not vary like the Blt1-mCherry intensity along the plasma membrane in the middle focal plane of these cells (Figure 4D). These measurements extend a previous report over a narrower range of cell lengths (Pan et al., 2014). We conclude that during the G_2/M phase transition of the cell cycle the local Pom1 concentration in the broad band does not control the variation in node number with cell size.

We used the *nmt81* (no message in thiamine) thiamine-repressible promoter (Maundrell, 1993) to control the expression of Pom1 and measured the effects on the cells and their cytokinesis nodes (Figure 5). Pom1 expression was lowest under repressing conditions (EMM5S with thiamine) and 3 times higher than wild-type cells grown in EMM5S without thiamine for 40 h (Figure 5A). The intensity of mEGFP-Pom1 in the broad band along the plasma membrane (Figure 5B) and the length of cells undergoing the G_2/M transition (Figure 5C) increased with the average concentration of Pom1 in the cells. The Blt1-mCherry intensity per pixel in the broad band also increased with the Pom1 concentration (Figure 5D), but the unitary node fluorescence measured with Blt1-mCherry did not change (Figure 5E). The width of the broad band of nodes did not change with the total Pom1 (Figure 5F). Therefore, the density of nodes in the broad band increased modestly with the cellular Pom1 concentration as the broad band occupied a smaller fraction of the cell length (Figure 5G). The ratio of the broad band width to the cell length decreased with the total cellular Pom1, indicating that Pom1 controls the width of the broad band (Figure 5H) as expected from previous work (Allard et al., 2019).

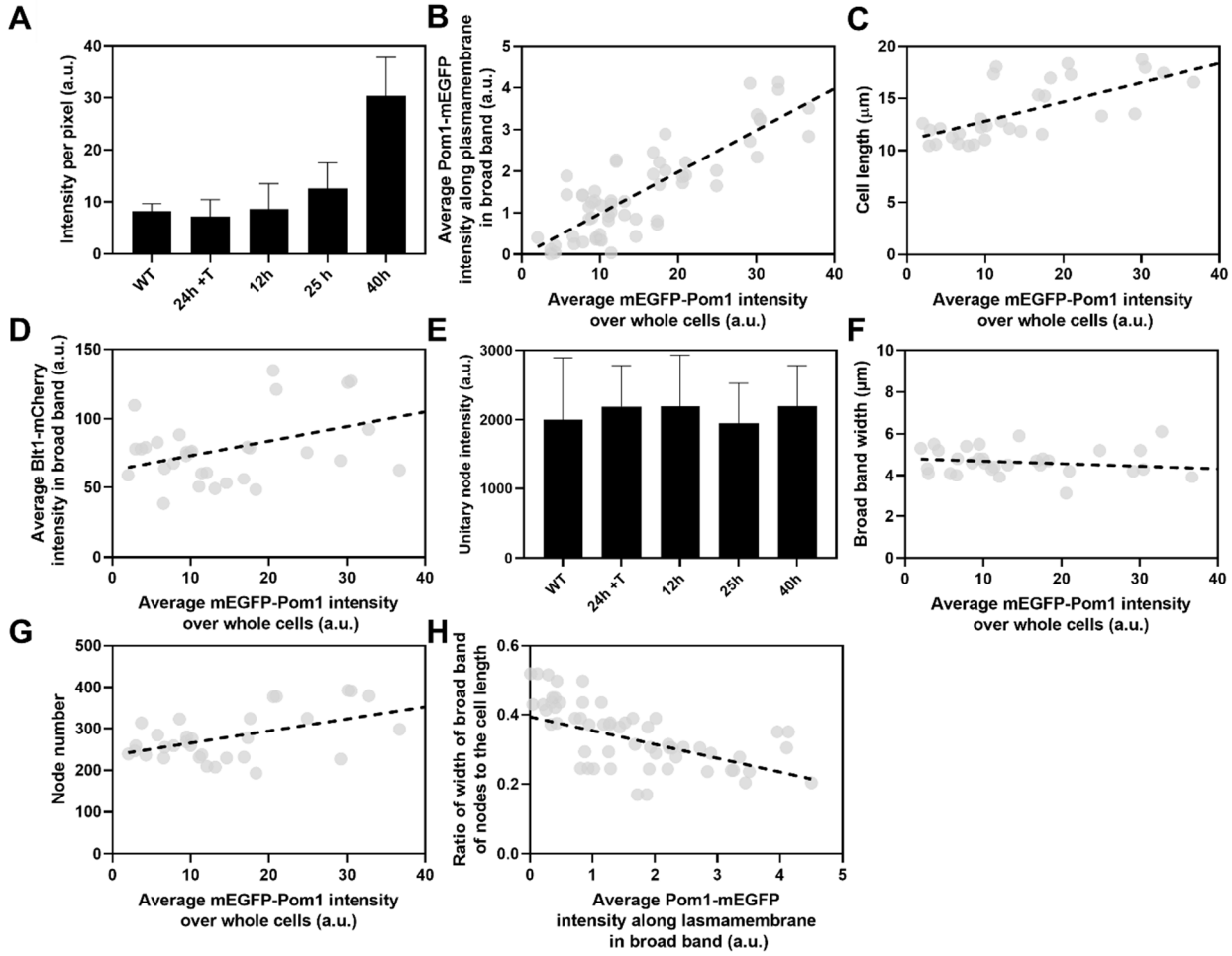

Figure 5. Influence of Pom1 concentration on cell size and numbers of cytokinesis nodes. Expression of mEGFP-Pom1 in cells from the *nmt81* promoter under three conditions: in EMM5S with 5 µg/ml thiamine for 24 h (n = 6 cells) to suppress expression or in EMM5S without thiamine to promote expression for 12 h (n = 6 cells), 25 h (n = 8 cells) or 40 h (n = 8 cells). Grey symbols show individual cells. (A) mEGFP-Pom1 expression under four conditions measured as fluorescence intensity per pixel of mEGFP-Pom1 over the whole cells. (B) Average mEGFP-Pom1 intensity along the plasma membrane in the broad band of nodes in the middle focal plane of the cells as a function of average mEGFP-Pom1 intensity in whole cells. The slope of the linear regression (black dotted line) is significantly nonzero ($P < 0.0001$; $R^2 = 0.7$). (C) Cell length as a function of average mEGFP-Pom1 intensity in whole cells. The slope of the linear regression (black dashed line) is significantly nonzero ($P < 0.0001$; $R^2 = 0.5$). (D) Blt1-mCherry intensity per pixel in node broad band as a function of average mEGFP-Pom1 intensity in whole cells. The slope of the linear regression (black dotted line) is significantly nonzero ($P = 0.01$; $R^2 = 0.2$). (E) Unitary node intensities measured by using Blt1-mCherry in WT cells and cells expressing different levels of Pom1. Error bars are SD, $P = 0.001$ as determined by Tukey's multiple comparison test. (F) Width of the broad band region as a function of average mEGFP-Pom1 intensity in whole cells. The slope of the linear regression (black dashed line) is significantly zero ($P = 0.3$; $R^2 = 0.04$). (G) Node number as a function of average mEGFP-Pom1 intensity in whole cells. The slope of the linear regression (black dotted line) is significantly nonzero ($P = 0.0017$; $R^2 = 0.3$). (H) Ratio of width of broad band of nodes to the cell length as a function of average mEGFP-Pom1 intensity along the plasma membrane in the broad band of nodes in the middle focal plane of the cells. The slope of the linear regression (black dotted line) is significantly nonzero ($P = 0.0001$; $R^2 = 0.4$).

Does Cdr2 control the number of nodes?

The kinase Cdr2 is the scaffold protein for interphase type 1 nodes, which cluster around the middle of the cell and later merge with type 2 nodes to form cytokinesis nodes. To determine whether the numbers of cytokinesis nodes depend on the concentration of Cdr2, we replaced the Cdr2 promoter in the *S. pombe* genome with the *nmt81* (no message in thiamine) thiamine-repressible promoter (Maundrell, 1993). To quantify Cdr2 expression in these cells the N-terminus of Cdr2 was tagged with mEGFP. This strain also had a C-terminal RFP tag on Sad1 to mark SPBs and a C-terminal mCherry tag on Blt1 to locate and count cytokinesis nodes. Thiamine suppressed the expression of mEGFP-Cdr2 from the *nmt81* promoter while growth without thiamine produced mEGFP-Cdr2 concentrations higher than wild-type cells (Figure 6A).

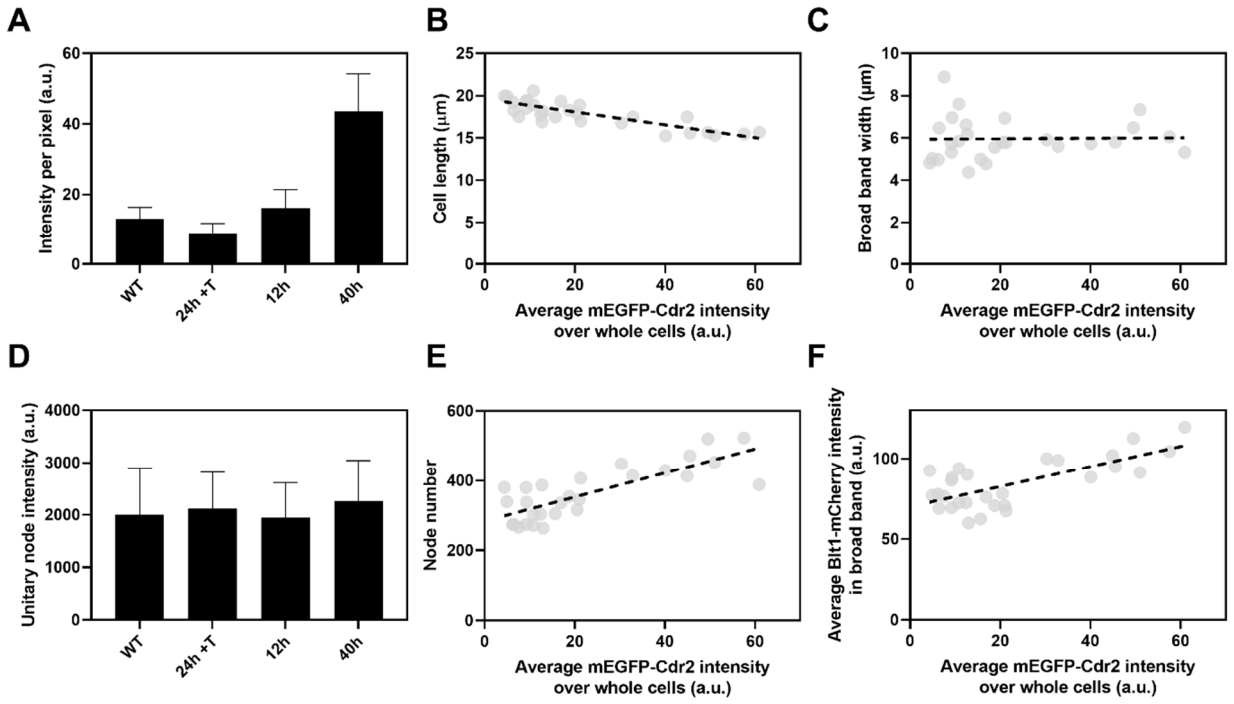

Figure 6. Influence of Cdr2 concentration on cell size and the number of cytokinesis nodes. Expression of mEGFP-Cdr2 in wild-type cells (n = 11 cells) and from the *nmt81* promoter under three conditions: in EMM5S with 5 µg/ml thiamine for 24 h (n = 10 cells) to suppress expression or in EMM5S without thiamine to promote expression for 12 h (n = 9 cells) or 40 h (n = 9 cells). Average fluorescence intensities per pixel were measured in sum projection images over whole cells. Grey symbols show individual cells. (A) Average mEGFP-Cdr2 fluorescence intensities per pixel over the whole cells under four conditions. (B) Cell length as a function of average mEGFP-Cdr2 intensity over whole cells. The slope of linear regression (black dashed line) is significantly nonzero ($P < 0.0001$; $R^2 = 0.6$). (C) Width of the broad band of nodes as a function of average mEGFP-Cdr2 intensity over whole cells. The slope of the linear regression (black dashed line) is significantly zero ($P = 0.9$; $R^2 = 0.0004$). (D) Unitary node intensities measured by using Blt1-mCherry in WT cells and cells expressing different levels of Cdr2p. (E) Node number as a function of average mEGFP-Cdr2 intensity over whole cells. The slope of the linear regression (black dotted line) is significantly nonzero ($P < 0.0001$; $R^2 = 0.6$). (F) Blt1-mCherry intensity per pixel in the broad band area as a

function of average mEGFP-Cdr2 intensity over whole cells. The slope of the linear regression (black dotted line) is significantly nonzero ($P < 0.0001$; $R^2 = 0.7$).

The length of the cells as they entered mitosis decreased with the concentration of mEGFP-Cdr2 (Figure 6B), but the width of the broad band of nodes did not change (Figure 6C). The average unitary node intensity measured with Blt1-mCherry in cells grown for 12, 25, or 40 h in EMM5S media and 24 h in EMM5S+thiamine did not differ from wild-type cells (Figure 6D). Both the intensity of Blt1-mCherry per pixel in the broad band and the number of cytokinesis nodes increased with the expression of mEGFP-Cdr2 (Figure 6E-F). We conclude that the cellular concentration of Cdr2 has a modest effect on the number and density of cytokinesis nodes and the size of cells entering mitosis but not the width of the broad band of nodes.

Discussion

The cytokinesis node cycle

During early G_2 the decline in SIN activity allows about half of the cell's constant concentration Cdr2 molecules to assemble from cytoplasmic pools into type 1 nodes around the equator of each new daughter cell (Akamatsu et al., 2017; Pu et al., 2015). These stationary type 1 nodes are anchored to the plasma membrane (Akamatsu et al., 2014) and capture diffusing type 2 nodes to form cytokinesis nodes. Cytokinesis nodes accumulate Myo2, formin Cdc12, and other proteins required to form a contractile ring by a search, capture, pull and release mechanism (Vavylonis et al., 2008). Previous work was not clear on the numbers of cytokinesis nodes or the mechanisms that set these numbers.

Numbers of cytokinesis nodes

Using Airyscan imaging we measured the number of cytokinesis nodes in *S. pombe* and discovered that the number of nodes is proportional to cell size. Previous studies underestimated the number of cytokinesis nodes due to limitations of imaging techniques and/or methods used to choose nodes (Akamatsu et al., 2014, 2017; Allard et al., 2018; Deng & Moseley, 2013; Laplante, Berro, et al., 2016; Lenz et al., 2012; Pan et al., 2014; Vavylonis et al., 2008; Willet et al., 2019). Conventional confocal microscopy cannot resolve closely spaced nodes, so confocal images give the impression that cytokinesis nodes vary considerably in size and fluorescence intensity. Several studies considered only the largest nodes when estimating their numbers. On the other hand, super-resolution single-molecule localization microscopy showed that nodes are

uniform in size and composition (Laplante, Huang, et al., 2016). However, the method cannot make a 3D reconstruction of live cells to count the total number of nodes, so the numbers were estimated by extrapolation.

Airyscan imaging overcomes these limitations by allowing 3D reconstructions of live cells at a higher resolution than conventional confocal microscopes. We imaged 40 z- slices covering the entire thickness of the cells and used the method of Akamatsu et al. (2017) to count cytokinesis nodes. The first step was to measure the average fluorescence intensity of a sample of unitary nodes marked with Blt1-mEGFP (Figure 2D). The Airyscan microscope resolved unitary nodes better than the confocal microscope used by Akamatsu (Figure 1), so we observed a single peak in the distribution of fluorescence intensities rather than multiple peaks of fluorescence intensity arising from overlapping unitary nodes. These unitary nodes move closer to each other to form binary and multiples of unitary nodes and eventually coalesce into a contractile ring. The second step was to measure the total Blt1-mEGFP fluorescence in the broad band of nodes in the cortex around the equator of the cell, correcting for background cytoplasmic fluorescence. Dividing the total Blt1-mEGFP fluorescence in the broad band by the average fluorescence of a unitary node gave the number of nodes, ~200 unitary nodes in wild-type fission yeast cells.

Similar measurements on contractile rings yielded ~150 cytokinesis nodes in wild-type cells. Therefore, about 75% of total cytokinesis nodes (~200) are incorporated into contractile rings. This may be related to the observation that 10 min before spindle pole bodies divide, 75% of cytokinesis nodes contained markers of both type 1 and type 2 nodes (Akamatsu et al., 2014) when they begin to accumulate Myo2, IQGAP Rng2, F-BAR Cdc15, and formin Cdc12 (Wu 2003). During 10-15 min after spindle pole bodies separate, cytokinesis nodes containing these proteins and Blt1 condense into a contractile ring (Vavylonis et al., 2008; Wu et al., 2006). The type 1 node scaffold protein Cdr2 leaves the contractile ring as it forms (Akamatsu et al., 2014). Anillin Mid1 is released from the fully formed contractile rings as unconventional myosin-II Myp2 joins the ring (Wu 2003). It is possible that the 25% of cytokinesis nodes lacking Cdr2 are left behind when the contractile ring forms because they failed to grow actin filaments or were deficient in Myo2, which are required for contractile ring formation.

Our approach may be useful to expand studies on how the density of nodes marked with Cdr2 senses surface area, activates cyclin-dependent kinase Cdk1 through inhibitory phosphorylation of *wee1,* and promotes the transition into mitosis (Facchetti, Knapp, Flor-Parra, et al., 2019; Pan et al., 2014; Russell & Nurse, 1987; Simanis & Nurse, 1986). Rather than measuring the total intensity of Cdr2 around the equator (Facchetti, Knapp, Flor-Parra, et al., 2019; Pan et al., 2014; Russell & Nurse, 1987; Simanis & Nurse, 1986) or counting only bright nodes (Pan et al., 2014), we measured the number of unitary nodes marked with Blt1 and found that their density was constant over a wide range of cell sizes (Figure 3K) where the node numbers were proportional to cell size (Figure 3J). Using our method to count unitary nodes marked with Cdr2 or Blt1 may provide further insights into the relation of node numbers to the timing of cell division.

Node number scales with cell size

Starting from the observation that the number of interphase nodes increases with the two-fold increase in cell size during interphase (Akamatsu et al., 2017; Allard et al., 2018; Deng & Moseley, 2013; Pan et al., 2014), we measured the number of cytokinesis nodes in mutant cells that varied 5-fold in size as they entered mitosis (Figure 3). The average fluorescence intensity of the unitary nodes was the same in wild-type and these mutant cells except for the tiny *wee1-50* mutant cells (Figure 3G). The surface density of nodes in the broad band was also constant at the time cells entered mitosis, while their numbers increased in proportion to the size of the cells and the surface area of the broad band (Figure 3J-K). The total broad band fluorescence and therefore the total number of nodes increased with cell size (Figure 3H-I).

Influence of the kinases Pom1 and Cdr2 on the broad band of cytokinesis nodes

We investigated the roles of Pom1, the kinase that restricts type 1 nodes from the poles of cells, and Cdr2, the kinase and scaffold protein for type 1 nodes, in setting the number of cytokinesis nodes. Pom1 forms a gradient from the cell tips to their middles and phosphorylates Cdr2 at multiple sites. Phosphorylation of one site reduces Cdr2 oligomerization and membrane binding at the poles, while phosphorylation of another site inhibits Cdr2 from phosphorylating the Wee1 kinase (Bhatia et al., 2014; Deng & Moseley, 2013; Martin & Berthelot-Grosjean, 2009; Moseley et al., 2009; Rincon et al., 2014). However, both *cdr2*Δ and *pom1*Δ cells form nodes and complete cytokinesis, although the cleavage site is off-center in *pom1*Δ cells because they

only exclude nodes from one pole by an unknown mechanism (Martin & Berthelot-Grosjean, 2009; Moseley et al., 2009).

Both the Pom1 concentration along the plasma membrane around the equator and the densities of cytokinesis nodes were similar over a five-fold range of cell sizes and cytokinesis node numbers (Figure 4C). This is consistent with the observations of Pan et al. (2014), who found that the Pom1 concentration along the equatorial plasma membrane of wild-type cells did not vary over a two-fold range of cell sizes and interphase node numbers. Thus, the scaling of node numbers with cell size is not a consequence of differences in Pom1 in the broad band. Furthermore, Pan et al. (2014) also reported that total Cdr2 and Cdr2 in nodes increased with cell size during the cell cycle in cells with or without Pom1. This is very strong evidence that Pom1 does not control type 1 node formation directly, rather as we explain below, Pom1 controls the node number indirectly via its influence on cell size.

Although neither Cdr2 and Pom1 control the scaling of node number with cell size, both can influence the number and density of cytokinesis nodes in the broad bands of mitotic cells. Artificially varying the total cellular concentration of Pom1 revealed the following dependencies as cells entered mitosis: the lengths of the cells (Figure 5C), the concentration of Pom1 along the plasma membrane in the broad band (Figure 5B), and the numbers of nodes (Figure 5G) all increased with the cellular concentration of Pom1, while both the fluorescence of unitary nodes (Figure 5E) and the width of the broad band (Fig 5F) were constant. Therefore, the density of nodes increased (Figure 5F) as the broad band occupied a smaller fraction of the cell length (Fig 5H) at high concentrations of Pom1. The numbers of nodes in cells expressing high Pom1 concentrations exceeded the numbers in cells of similar lengths and normal Pom1 concentrations (Figure 3I).

On the other hand, cells expressing low concentrations of Pom1 divided at shorter lengths (Figure 5C) with fewer nodes (Figure 5G) than cells with high Pom1 concentrations. These numbers were higher than in cells of a given length with normal Pom1 levels (Figure 3G).

Artificially increasing the total cell concentration of Cdr2 (Figure 6) reduced cell length at the time of division (Figure 6B) but did not change the width of the broad band of nodes (Figure 6C), so the broad band occupied a larger fraction of the cell surface. High Pom1 concentrations had the opposite effects on cell size (Figure 5C) and broad band width (Figure

5F). On the other hand, the number of nodes increased with the concentration of Cdr2 (Figure 6E). The short cells expressing high Cdr2 concentrations had almost double the number of nodes in their slightly wider broad bands than cells of similar lengths with wild-type levels of Cdr2 (Figure 3I). Longer cells expressing low concentrations of Cdr2 had numbers of nodes similar to cells of the same lengths in Figure 3I. The plot of node number vs. Cdr2 concentration extrapolates to more than 200 nodes when the Cdr2 concentration is zero (Figure 6E), as expected for cells longer than wild-type cells at division (Figure 6B). Therefore, Cdr2 can drive node numbers above the basal level of about 200.

Mechanisms

Cell size dominates in setting the basal number of nodes: Low SIN activity during interphase is a prerequisite for the assembly of type 1 interphase nodes (Pu et al., 2015), but cell size has a dominant influence in setting the number of nodes in wild-type cells. Accordingly, as cells grow, the number of interphase nodes doubles as they mature into cytokinesis nodes. A limiting amount of an essential node protein might set the number of nodes, but only about half of each of the known node proteins assemble into nodes (Akamatsu et al., 2017). Alternatively, a cell-size-dependent posttranslational modification of one of these proteins may limit the number of nodes. Phosphorylation of the type 2 node scaffold protein Cdr2 by Pom1 is a candidate mechanism, but deletion of Pom1 does not affect the number of nodes (Bhatia et al., 2014; Pan et al., 2014). Nodes turn over continuously, so the rates of node formation and turnover must have a strong influence on their numbers. However, we do not yet know whether one protein at a time or whole nodes turn over or how this process is controlled. All these options are attractive subjects for future research.

Pom1 and Cdr2 modulate a basal number of nodes: We find that cell size is the primary determinant of the number of nodes (Figure 3H) but that the cellular concentrations of the Cdr2 and Pom1 kinases can independently influence cell size and drive the number of nodes above a baseline (Figure 7). The modulating effect of the two kinases is seen in plots of node number vs. the concentrations of either kinase, which intercept the y-axis well above zero (Figures 3H, 5G, and 6E). The presence of a basal number of nodes is expected, since cells without either Cdr2 or Pom1 form cytokinesis nodes (Almonacid et al., 2009; Martin & Berthelot-Grosjean, 2009;

Moseley et al., 2009). We propose that interactions of Pom1 and Cdr2 modulate the numbers of cytokinesis nodes through their effects on cell size.

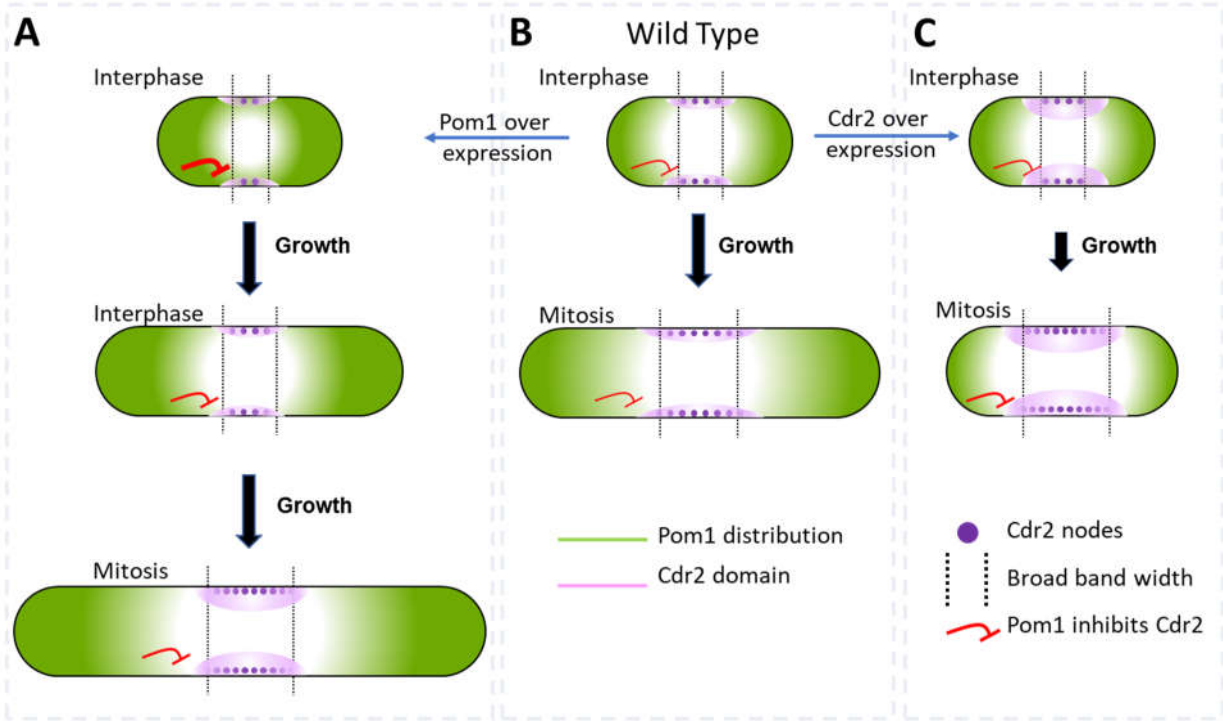

Figure 7. Factors that influence cell size and the broad band of cytokinesis nodes in (B) wild-type cells and cells overexpressing (A) Pom1 or (C) Cdr2. The gradient of Pom1 along the cell plasma membrane is shown in green. The distribution of Cdr2 on the plasma membrane is shown in magenta and called the Cdr2 domain. Purple spheres show the density of Cdr2 nodes. Blunt end red lines show the inhibitory action of Pom1 on Cdr2, with the line thickness showing the strength. Lengths of black arrows show the time spent growing. The two dotted lines across the middles of the cells show the borders of the broad band of nodes.

Pom1 regulates node localization by phosphorylating Cdr2, which reduces its oligomerization and membrane binding (Bhatia et al., 2014; Rincon et al., 2014). This direct effect of Pom1 on Cdr2 is one way the gradient of Pom1 from the poles of the cell can restrict nodes to a broad band around the equator (Figure 7B). As cells grow, the overlap of the Pom1 gradient with Cdr2 in the middle of the cell decreases.

In addition, Pom1 regulates cell size at the time of division through a series of three inhibitory phosphorylation reactions: Pom1 phosphorylation inhibits the kinase activity of Cdr2; Cdr2 phosphorylates and inhibits the Wee1 kinase; Wee1 phosphorylates inhibitory sites on Cdk1, the master mitotic kinase that promotes entry into mitosis (Allard et al., 2018; Breeding et al., 1998; Russell & Nurse, 1987). As cells grow, the influence of Pom1 on Cdr2 and Wee1

diminishes, contributing to the activation of Cdk1 and the transition into mitosis (Figure 7B) (Allard et al., 2018, 2019; Martin & Berthelot-Grosjean, 2009; Moseley et al., 2009).

Based on these mechanisms, overexpression of Cdr2 might increase the number of nodes (Figures 6E and 7C) by mass action. In addition, mass action may drive Cdr2 to inhibit enough Wee1 to promote premature mitosis, resulting in short daughter cells (Figure 6B) with more nodes packed more densely in a broad band of normal width (Figures 6C, 6E, and 7C).

Unexpectedly, the number of nodes also increases with the Pom1 concentration (Figure 5G). Based on the Pom1 to Cdk1 pathway, one expects high concentrations of Pom1 to inhibit assembly of Cdr2 into node. However, inhibiting Cdr2 results in high Wee1 activity that inhibits Cdk1, delays the cell cycle, and allows cells to grow longer (Figure 7A). The dominant effect of cell size on driving node formation produces more nodes (Figure 5C).

Pom1 and Cdr2 influence the width of the broad band and density of nodes: Wild-type cells form type 1 nodes around the daughter nuclei and use a gradient of Pom1 from the poles to confine these nodes to the equator throughout interphase (Figure 7B). As cells elongate during interphase, three parallel events result in two-fold longer cells with twice the number of nodes located in a two-fold wider broad band ready for mitosis. First, the Pom1 concentration on the plasma membrane is low in a zone in the middle of the cell that widens in proportion to a wide range of cell sizes (Figures 3J, 4C and 7B) (Bhatia et al., 2014; Pan et al., 2014). Second, the total number of nodes marked with Blt1 (Figure 3H) or Cdr2 (Bhatia et al., 2014; Pan et al., 2014) in this broad band increases with cell size in cells with or without Pom1 (Bhatia et al., 2014; Pan et al., 2014). Third, the broad band widens in proportion to cell size (Figure 3J), so the surface density of cytokinesis nodes is independent of the cell size (Figure 3K). Two additional factors contribute to limiting nodes to the equator. One is the uncharacterized activity that excludes nodes from one pole in the absence of Pom1 (Martin & Berthelot-Grosjean, 2009; Moseley et al., 2009). The other is anillin, Mid1, given that nodes spread over the entire plasma membrane in *mid1*Δ cells (Saha & Pollard, 2012)

The concentrations of Pom1 and Cdr2 to Pom1 also influence the width of the broad band and the density of nodes therein (Figure 7). Overexpression of Cdr2 drives both node formation and premature cell division, while the natural level of Pom1-driven inhibition from the poles does not allow space for new nodes at the edges of the broad band, so the surface density of

cytokinesis nodes is higher (Figure 7C). Cells overexpressing Pom1 also have a higher density of nodes around their equators owing to more nodes (Figure 5G) in broad bands of normal widths (Figure 5F). Like short wild-type interphase cells (Figure 7B), overexpression of Pom1 increases its concentration in the middle of cells (Figure 5B) and suppresses the spread of the broad band in spite of delayed mitosis increasing the length of these cells (Figures 5C and 7A).

Influence of cell shape: The shape of the cell can also influence the number of nodes. For example, the wide but short *rga4Δ* mutant cells lacking the RhoGAP Rga4 are normal in many ways (unitary node intensity, numbers, and densities of nodes for their lengths) but due to their large diameters, they are an outlier with fewer cytokinesis nodes than expected for cells with their volume. In addition, the gradient of Pom1 from the cell tips is steeper in *rga4Δ* mutant cells than wild-type cells and the Blt1-mCherry+Sad1RFP fluorescence was spread more widely across the middle of *rga4Δ* mutant cells than in wild-type or other strains (Figure 4B, second and third panels from the top).

Methods and Materials

Yeast strains

Table 1 lists the strains used in this work. We used standard methods for *S. pombe* growth and genetics (Moreno et al., 1991). We made most observations on a strain with spindle pole bodies (SPBs) marked by Sad1–RFP, and nodes marked by Blt1-mEGFP (Goss et al., 2014). The sequences encoding the fluorescent proteins were incorporated into the haploid genome, so all copies of these proteins were tagged. The yeast strains *rga2Δ* (FC3158) and *rga4Δ* (FC3157) were a kind gift from the laboratory of Prof. Fred Chang (University of California, San Francisco). All the other strains were obtained from laboratory stocks or by crossing laboratory stock strains. Strains were confirmed by growth on selective media and microscopy. Except for Figures 5 and 6, cells were grown in YE5S medium for 24 h at 25°C and then overnight in synthetic EMM5S medium at 25°C before imaging.

To control the expression of Cdr2 and Pom1 (Figures 5 and 6), we inserted by homologous recombination the weak *nmt81* promoter along with mEGFP upstream of the open reading frames for Cdr2 or Pom1 in their chromosomal loci. Cells were grown in EMM medium for 25 h at 25°C to induce moderate expression or 40 h at 25°C to over-express mEGFP-Cdr2 or mEGFP-Pom1. Cells were grown in 5 μg/ml thiamine for >24 h at 25°C to repress the

expression of these two fusion proteins. The OD_{595} of the cultures was kept below 0.6 over the entire period.

Table 1. Strains used in this study

Strain	Genotype	Source
WS40	h- blt1-mEGFP:KanMX6 sad1-RFP:KanMX6 ade6-M21X leu1-32 ura4-Δ18	Laboratory Stock
WS46	h- *cdc25-22* blt1-mEGFP:KanMX6 sad1-RFP:KanMX6 ade6-M21X leu1-32 ura4-Δ18	This study
WS47	h- wee1-50 blt1-mEGFP:KanMX6 sad1-RFP:KanMX6 ade6-M21X leu1-32 ura4-Δ18	This study
WS51.1	h- *rga2*Δ blt1-mEGFP:KanMX6 sad1-RFP:KanMX6 ade6-M21X leu1-32 ura4-Δ18	This study
WS52.1	h- *rga4*Δ blt1-mEGFP:KanMX6 sad1-RFP:KanMX6 ade6-M21X leu1-32 ura4-Δ18	This study
WS59	h- pom1-GFP kanMX6 blt1-mCherry natMX6 sad1-mRFP kanMX6 ade6-M21X leu1-32 ura4-Δ18	Laboratory Stock
WS54	h- *rga2Δ* pom1-GFP kanMX6 blt1-mCherry natMX6 sad1-mRFP kanMX6 ade6-M21X leu1-32 ura4-Δ18	This study
WS55	h- *rga4Δ* pom1-GFP kanMX6 blt1-mCherry natMX6 sad1-mRFP kanMX6 ade6-M21X leu1-32 ura4-Δ18	This study
WS56	h- *cdc25-22* pom1-GFP kanMX6 blt1-mCherry natMX6 sad1-mRFP kanMX6 ade6-M21X leu1-32 ura4-Δ18	This study
WS57	h- *wee1-50* pom1-GFP kanMX6 blt1-mCherry natMX6 sad1-mRFP kanMX6 ade6-M21X leu1-32 ura4-Δ18	This study
WS70	h- HygMX6-Pnmt81-mEGFP-Pom1 blt1-mCherry natMX6 sad1-mRFP kanMX6 ade6-M21X leu1-32 ura4-Δ18	This study
WS71	h- KanMX6-Pnmt81-mEGFP-Cdr2 blt1-mCherry natMX6 sad1-mRFP kanMX6 ade6-M21X leu1-32 ura4-Δ19	This study

Airyscan microscopy

Imaging was performed on LSM 880 laser scanning confocal microscope (ZEISS) equipped with 100X Plan Apochromatic 1.46 NA oil objective, an Airyscan super-resolution module, GaAsP detectors, and Zen Black acquisition software (ZEISS). We acquired 40 Z-slices with step size 170 nm covering the entire volume of a cell. Pixel size was 41 nm by 41 nm by 170 nm. Images were collected with pixel dwell time 1.02 μs and image size of 520 x 520 pixels corresponding to

22 × 22 μm. Cells were imaged with 488 nm laser and BP 420-480 excitation /BP 495-620 emission filters for mEGFP; and 561 nm laser and BP 495-550 excitation /LP 570 emission filters for RFP. The pixel dwell time, laser intensity, and detector gain were kept low to avoid saturation and photobleaching during the image acquisition. To increase signal-to-noise ratio and resolution, acquired images were processed by 3D Airyscan filter strength 7.0 with Zen Black software.

We identified cytokinesis nodes as spots of Blt1-mEGFP fluorescence around the equator of cells with two SPBs marked by Sad1–RFP, indicating that the cells were in mitosis. We identified and measured the fluorescence intensity of unitary cytokinesis nodes using the following procedure to process the fluorescent images. First, we used ImageJ software to make a maximum intensity projection from 40 Z-slices of Airyscan images containing all of the fluorescence spots in the broad band of a cell (Figure 2A). These spots varied considerably in size and brightness depending on the number of 'unitary nodes' clustered in a diffraction-limited spot (Akamatsu et al., 2017; Laplante, Huang, et al., 2016). We searched for dim spots and marked their X-Y positions. Then we inspected the fluorescence along the Z-axis at these X-Y positions in 40 Z- slices. To qualify as a unitary node, a spot had to satisfy two conditions: 1) the fluorescence of a spot was present within a circle 12 pixels (~0.5 μm) in diameter; and 2) the fluorescence of a spot was present in 7 or fewer consecutive Z-slices with a peak in the middle slice and diminishing towards both sides. This middle slice was designated as the Z-axis position of the unitary node. The X-Y-Z positions of each node were stored in the ROI manager of ImageJ software and exported to MATLAB using the add-on @ReadImageJROI developed by Dylan Muir (2020). We developed a MATLAB code for further analysis. We sum projected the 7 z-slices containing the unitary node and measured the total fluorescence intensity within circle 12-pixels in diameter the X-Y position of the node (Figure 2B, black dotted circle). From the same sum-projected image we measured the average cytoplasmic fluorescence from 8 circles 12-pixels in diameter from regions of cytoplasm near the cell tips where nodes were absent (Figure 2B, blue dotted circles). We subtracted this average cytoplasmic fluorescence from the node fluorescence to remove the background to obtain fluorescence of a unitary node.

To obtain the total fluorescence of a broad band of nodes, we sum projected 40 Z- slices of Airyscan images and measured the fluorescence of an ROI drawn around the broad band of

nodes (Figure 2C, Red dashed line area). The mean pixel intensity from polygonal ROIs from each cell tip (Figure 2C Yellow dashed line) was averaged and multiplied by the number of pixels in the broad band ROI to calculate the background fluorescence in the volume of the broad band of nodes. This value was subtracted from the fluorescence in the broad band of nodes to remove the background. To estimate the number of nodes in a cell we divided the total fluorescence of the broad band of nodes after subtracting the background by the average total fluorescence of individual unitary nodes after subtracting the background.

Confocal microscopy

To compare the confocal and Airyscan imaging shown in Figure 1 we obtained confocal images using the same Airyscan detector. To make and improve the signal-to-noise ratio comparable to Airyscan microscopy we used the pinhole 0.6 AU, 8X averaging, linear constrained iterative deconvolution, and twice the 488 nm laser intensity implemented in Airyscan imaging. We acquired 20 Z-slices with step size 340 nm covering the entire fluorescence of a cell with pixel size 82 nm by 82 nm. Images were processed for linear constrained iterative deconvolution using the ImageJ plugin 'Deconvolution'.

To determine the Pom1 localization in Figure 5, we used an Olympus IX-71 microscope with a 100×, numerical aperture (NA) 1.4 Plan Apo lens (Olympus) and a CSU-X1 (Andor Technology) confocal spinning-disk system equipped with an iXON-EMCCD camera (Andor Technology). We used Coherent OBIS 488 nm LS 20 mW and OBIS 561 nm LS 20 mW lasers for excitation. Images were acquired using Micromanager 1.4 (Edelstein et al., 2014).

We acquired 15 Z-slices covering the fluorescence of entire cells every 2-5 min with 0.5 μm spacing between slices; 22 μW 561 nm laser power (measured after the objective) and 50 ms exposures; 89 μW 488 laser power and 200 ms exposures. Images were sum projected and corrected for camera noise and uneven illumination. Photobleaching was compensated by choosing a small ROI in both channels that was present in another nondividing cell throughout the acquisition and using the Fiji plugin 'Bleach correction' for Exponential Fitting.

We studied cytokinesis nodes in cells during the interval between SPB separation and the formation of the contractile ring. The intensity per pixel of an ROI where no cells were present was subtracted from both channels to remove substrate background intensity. Then a line equal to cell width was drawn along the length of the cell, and a line profile was obtained using the

ImageJ -Plot profile plugin, which generated a graph of intensity per pixel across the width of cell vs the cell length. The intensity per pixel of wild-type cells not expressing a fluorescent protein was subtracted from each point to remove auto-fluorescence. To measure the distributions of the fluorescence from Pom1-GFP or Blt1-mCherry plus Sad1-RFP at different phases of cell cycles of wild-type, *wee1-50,* and *cdc25-22* mutant cells, we plotted the intensities per pixel across the width of cell vs the cell length across the cell cycle (Figure 4A).

For each strain except in *cdc25-22* mutant strain, 10-12 line profiles were obtained as above and aligned at the centers of the cells before calculating average intensities and standard deviations. The temperature-sensitive *cdc25-22* mutant cells were grown at the restrictive temperature of 36°C for 4 h and released for imaging at 22°C. These cells had a homogeneous distribution of Pom1 in the cytoplasm but higher on one side of the nucleus than the other. In these cells, the line profiles were flipped so the higher concentration of Pom1 was at one end and aligned on their cell centers before averaging and calculating the standard deviations of the line profiles (Figure 4B). We measured the width of the broad band of cytokinesis nodes as the zone where the Blt1-mEGFP signal was >20% of the peak value.

We outlined manually whole cells or the broad band area and used the ImageJ plugin 'Measure' to measure the Mean intensity in these areas from the intensity per pixel calculated as the total intensity in all the pixels in a region divided by the number of pixels, which is equivalent to the density (Figure 5 and 6).

In Figure 4C the Pom1-mEGFP intensity along the equatorial plasma membrane was measured from the confocal images of the middle focal plane (thickness ~ 0.5 μm) of the cells after subtracting the average background intensity from the area where cells were absent in the same image. A rectangle 3 pixels wide (~ 0.4 μm) and as long as the broad band of nodes was manually drawn over the plasma membrane of cells in the image and used to calculate the Pom1-mEGFP intensity per pixel.

In Figure 5B, for the similar analysis as in Figure 4C, the mEGFP-Pom1 intensity was measured from the sum projected image of 3 consecutive middle focal planes (thickness ~ 0.5 μm) of the cells obtained by using Airyscan Imaging. To remove the background, the average pixel intensity from the area where cells were absent in the sum image was subtracted from the image. A rectangle 10 pixel wide (~ 0.4 μm) and as long as the broad band of nodes was manually drawn

over the plasma membrane of cells in the image and used to calculate the Pom1-mEGFP intensity per pixel in the broad band as shown in Figure 4C, inset.

Acknowledgments

Research reported in this publication was supported by the National Institute of General Medical Sciences of the National Institutes of Health under award number R01GM026132. The content is solely the responsibility of the authors and does not necessarily represent the official views of the National Institutes of Health. The authors thank Prof. Chang for the *rga4*Δ and *rga2*Δ cells.

Author contributions

Wasim Sayyad, Conceptualization, Data collection, and analysis; Writing—original draft, Writing—review and editing. Thomas D Pollard, Conceptualization, Writing—review and editing; Resources.

Author ORCIDs

Thomas D Pollard https://orcid.org/0000-0002-1785-2969

Wasim A Sayyad https://orcid.org/0000-0002-6064-2860

References

Akamatsu, M., Berro, J., Pu, K. M., Tebbs, I. R., & Pollard, T. D. (2014). Cytokinetic nodes in fission yeast arise from two distinct types of nodes that merge during interphase. *Journal of Cell Biology*, *204*(6), 977–988. https://doi.org/10.1083/jcb.201307174

Akamatsu, M., Lin, Y., Bewersdorf, J., & Pollard, T. D. (2017). Analysis of interphase node proteins in fission yeast by quantitative and superresolution fluorescence microscopy. *Molecular Biology of the Cell*, *28*(23), 3203–3214. https://doi.org/10.1091/mbc.e16-07-0522

Allard, C. A. H., Opalko, H. E., Liu, K.-W., Medoh, U., & Moseley, J. B. (2018). Cell size–dependent regulation of Wee1 localization by Cdr2 cortical nodes. *Journal of Cell Biology*, *217*(5), 1589–1599. https://doi.org/10.1083/jcb.201709171

Allard, C. A. H., Opalko, H. E., & Moseley, J. B. (2019). Stable pom1 clusters form a glucose-modulated concentration gradient that regulates mitotic entry. *ELife*, *8*, 1–27. https://doi.org/10.7554/eLife.46003

Almonacid, M., Moseley, J. B., Janvore, J., Mayeux, A., Fraisier, V., Nurse, P., & Paoletti, A. (2009). Spatial Control of Cytokinesis by Cdr2 Kinase and Mid1/Anillin Nuclear Export. *Current Biology*, *19*(11), 961–966. https://doi.org/10.1016/j.cub.2009.04.024

Bähler, J., & Pringle, J. R. (1998). Pom1p, a fission yeast protein kinase that provides positional information for both polarized growth and cytokinesis. *Genes and Development*, *12*(9), 1356–1370. https://doi.org/10.1101/gad.12.9.1356

Beach, J. R., Shao, L., Remmert, K., Li, D., Betzig, E., & Hammer, J. A. (2014). Nonmuscle myosin II isoforms coassemble in living cells. *Current Biology*, *24*(10), 1160–1166. https://doi.org/10.1016/j.cub.2014.03.071

Bhatia, P., Hachet, O., Hersch, M., Rincon, S. A., Berthelot-Grosjean, M., Dalessi, S., Basterra, L., Bergmann, S., Paoletti, A., & Martin, S. G. (2014). Distinct levels in Pom1 gradients limit Cdr2 activity and localization to time and position division. *Cell Cycle*, *13*(4), 538–552. https://doi.org/10.4161/cc.27411

Breeding, C. S., Hudson, J., Balasubramanian, M. K., Hemmingsen, S. M., Young, P. G., &

Gould, K. L. (1998). The cdr2+ gene encodes a regulator of G2/M progression and cytokinesis in Schizosaccharomyces pombe. *Molecular Biology of the Cell*, *9*(12), 3399–3415. https://doi.org/10.1091/mbc.9.12.3399

Coffman, V. C., Nile, A. H., Lee, I.-J., Liu, H., & Wu, J.-Q. (2009). Roles of Formin Nodes and Myosin Motor Activity in Mid1p-dependent Contractile-Ring Assembly during Fission Yeast Cytokinesis. *Molecular Biology of the Cell*, *20*(24), 5195–5210. https://doi.org/10.1091/mbc.E09-05-0428

Das, M., Wiley, D. J., Medina, S., Vincent, H. A., Larrea, M., Oriolo, A., & Verde, F. (2007). Regulation of Cell Diameter, For3p Localization, and Cell Symmetry by Fission Yeast Rho-GAP Rga4p. *Molecular Biology of the Cell*, *18*(6), 2090–2101. https://doi.org/10.1091/mbc.e06-09-0883

Deng, L., & Moseley, J. B. (2013). Compartmentalized nodes control mitotic entry signaling in fission yeast. *Molecular Biology of the Cell*, *24*(12), 1872–1881. https://doi.org/10.1091/mbc.E13-02-0104

Edelstein, A. D., Tsuchida, M. A., Amodaj, N., Pinkard, H., Vale, R. D., & Stuurman, N. (2014). Advanced methods of microscope control using μManager software. *Journal of Biological Methods*, *1*(2), e10. https://doi.org/10.14440/jbm.2014.36

Facchetti, G., Knapp, B., Chang, F., & Howard, M. (2019). Reassessment of the Basis of Cell Size Control Based on Analysis of Cell-to-Cell Variability. *Biophysical Journal*, *117*(9), 1728–1738. https://doi.org/10.1016/j.bpj.2019.09.031

Facchetti, G., Knapp, B., Flor-Parra, I., Chang, F., & Howard, M. (2019). Reprogramming Cdr2-Dependent Geometry-Based Cell Size Control in Fission Yeast. *Current Biology*, *29*(2), 350-358.e4. https://doi.org/10.1016/j.cub.2018.12.017

Fantes, P., & Nurse, P. (1977). Control of cell size at division in fission yeast by a growth-modulated size control over nuclear division. *Experimental Cell Research*, *107*(2), 377–386. https://doi.org/10.1016/0014-4827(77)90359-7

Goss, J. W., Kim, S., Bledsoe, H., & Pollard, T. D. (2014). Characterization of the roles of Blt1p in fission yeast cytokinesis. *Molecular Biology of the Cell*, *25*(13), 1946–1957.

https://doi.org/10.1091/mbc.e13-06-0300

Gu, Y., & Oliferenko, S. (2019). Cellular geometry scaling ensures robust division site positioning. *Nature Communications*, *10*(1). https://doi.org/10.1038/s41467-018-08218-2

Henson, J. H., Ditzler, C. E., Germain, A., Irwin, P. M., Vogt, E. T., Yang, S., Wu, X., & Shuster, C. B. (2017). The ultrastructural organization of actin and myosin II filaments in the contractile ring: New support for an old model of cytokinesis. *Molecular Biology of the Cell*, *28*(5), 613–623. https://doi.org/10.1091/mbc.E16-06-0466

Hickson, G. R. X., & O'Farrell, P. H. (2008). Rho-dependent control of anillin behavior during cytokinesis. *Journal of Cell Biology*, *180*(2), 285–294. https://doi.org/10.1083/jcb.200709005

J.M.MitchisonJ.Creanor. (1971). and J. CREANOR. *Experimental Cell Research*, *67*(2), 368–374. https://doi.org/10.1016/0014-4827(71)90421-6

Jourdain, I., Brzezińska, E. A., & Toda, T. (2013). Fission Yeast Nod1 Is a Component of Cortical Nodes Involved in Cell Size Control and Division Site Placement. *PLoS ONE*, *8*(1). https://doi.org/10.1371/journal.pone.0054142

Krakoff, I. H., Brown, N. C., & Reichard, P. (1968). *Inhibition Reductase of Ribonucleoside by Hydroxyurea1 Diphosphate*. 1559–1565.

Laplante, C., Berro, J., Karatekin, E., Hernandez-leyva, A., & Pollard, T. D. (2016). *Three myosins contribute uniquely to the assembly and constriction of the fission yeast cytokinetic contractile ring Caroline*. *25*(15), 1955–1965. https://doi.org/10.1016/j.cub.2015.06.018.Three

Laplante, C., Huang, F., Tebbs, I. R., Bewersdorf, J., & Pollard, T. D. (2016). Molecular organization of cytokinesis nodes and contractile rings by super-resolution fluorescence microscopy of live fission yeast. *Proceedings of the National Academy of Sciences*, *113*(40), E5876–E5885. https://doi.org/10.1073/pnas.1608252113

Lenz, M., Gardel, M. L., & Dinner, A. R. (2012). Requirements for contractility in disordered cytoskeletal bundles. *New Journal of Physics*, *14*. https://doi.org/10.1088/1367-2630/14/3/033037

Martin, S. G., & Berthelot-Grosjean, M. (2009). Polar gradients of the DYRK-family kinase Pom1 couple cell length with the cell cycle. *Nature*, *459*(7248), 852–856. https://doi.org/10.1038/nature08054

Moreno, S., Hayles, J., & Nurse, P. (1989). Regulation of p34cdc2 protein kinase during mitosis. *Cell*, *58*(2), 361–372. https://doi.org/10.1016/0092-8674(89)90850-7

Moreno, S., Klar, A., & Nurse, P. (1991). [56] Molecular genetic analysis of fission yeast Schizosaccharomyces pombe. In *Methods in Enzymology* (Vol. 194, Issue C, pp. 795–823). https://doi.org/10.1016/0076-6879(91)94059-L

Morrell, J. L., Nichols, C. B., & Gould, K. L. (2004). *The GIN4 family kinase , Cdr2p , acts independently of septins in fission yeast*. *1*. https://doi.org/10.1242/jcs.01409

Moseley, J. B., Mayeux, A., Paoletti, A., & Nurse, P. (2009). A spatial gradient coordinates cell size and mitotic entry in fission yeast. *Nature*, *459*(7248), 857–860. https://doi.org/10.1038/nature08074

Neumann, F. R., & Nurse, P. (2007). Nuclear size control in fission yeast. *Journal of Cell Biology*, *179*(4), 593–600. https://doi.org/10.1083/jcb.200708054

Nurse, P. (1990). Universal control mechanism regulating cell cycle timing of M-phase. *Nature*, *344*(April), 503–508. https://link.springer.com/content/pdf/10.1038/344503a0.pdf%0Ahttps://www.nature.com/articles/344503a0.pdf

Nurse, Paul. (1975). Genetic control of cell size at cell division in yeast. *Nature*, *256*(5518), 547–551. https://doi.org/10.1038/256547a0

Pan, K. Z., Saunders, T. E., Flor-Parra, I., Howard, M., & Chang, F. (2014). Cortical regulation of cell size by a sizer cdr2p. *ELife*, *2014*(3), 1–24. https://doi.org/10.7554/eLife.02040

Pu, K. M., Akamatsu, M., & Pollard, T. D. (2015). The septation initiation network controls the assembly of nodes containing Cdr2p for cytokinesis in fission yeast. *Journal of Cell Science*, *128*(3), 441–446. https://doi.org/10.1242/jcs.160077

Rincon, S. A., Bhatia, P., Bicho, C., Guzman-Vendrell, M., Fraisier, V., Borek, W. E., Alves, F.

de L., Dingli, F., Loew, D., Rappsilber, J., Sawin, K. E., Martin, S. G., & Paoletti, A. (2014). Pom1 regulates the assembly of Cdr2-Mid1 cortical nodes for robust spatial control of cytokinesis. *Journal of Cell Biology*, *206*(1), 61–77. https://doi.org/10.1083/jcb.201311097

Russell, P., & Nurse, P. (1986). cdc25+ functions as an inducer in the mitotic control of fission yeast. *Cell*, *45*(1), 145–153. https://doi.org/10.1016/0092-8674(86)90546-5

Russell, P., & Nurse, P. (1987). Negative regulation of mitosis by wee1+, a gene encoding a protein kinase homolog. *Cell*, *49*(4), 559–567. https://doi.org/10.1016/0092-8674(87)90458-2

Saha, S., & Pollard, T. D. (2012). Characterization of structural and functional domains of the anillin-related protein Mid1p that contribute to cytokinesis in fission yeast. *Molecular Biology of the Cell*, *23*(20), 3993–4007. https://doi.org/10.1091/mbc.E12-07-0536

Simanis, V., & Nurse, P. (1986). The cell cycle control gene cdc2+ of fission yeast encodes a protein kinase potentially regulated by phosphorylation. *Cell*, *45*(2), 261–268. https://doi.org/10.1016/0092-8674(86)90390-9

Tatebe, H., Nakano, K., Maximo, R., & Shiozaki, K. (2008). Pom1 DYRK Regulates Localization of the Rga4 GAP to Ensure Bipolar Activation of Cdc42 in Fission Yeast. *Current Biology*, *18*(5), 322–330. https://doi.org/10.1016/j.cub.2008.02.005

Tatebe, H., Shimada, K., Uzawa, S., Morigasaki, S., & Shiozaki, K. (2005). Wsh3/Tea4 is a novel cell-end factor essential for bipolar distribution of tea1 and protects cell polarity under environmental stress in S. pombe. *Current Biology*, *15*(11), 1006–1015. https://doi.org/10.1016/j.cub.2005.04.061

Vavylonis, D., Wu, J.-Q., Hao, S., O'Shaughnessy, B., & Pollard, T. D. (2008). Assembly Mechanism of the Contractile Ring for Cytokinesis by Fission Yeast. *Science*, *319*(5859), 97–100. https://doi.org/10.1126/science.1151086

Villar-Tajadura, M. A., Coll, P. M., Madrid, M., Cansado, J., Santos, B., & Pérez, P. (2008). Rga2 is a Rho2 GAP that regulates morphogenesis and cell integrity in S. pombe. *Molecular Microbiology*, *70*(4), 867–881. https://doi.org/10.1111/j.1365-

2958.2008.06447.x

Werner, M., Munro, E., & Glotzer, M. (2007). Astral Signals Spatially Bias Cortical Myosin Recruitment to Break Symmetry and Promote Cytokinesis. *Current Biology*, *17*(15), 1286–1297. https://doi.org/10.1016/j.cub.2007.06.070

Willet, A. H., DeWitt, A. K., Beckley, J. R., Clifford, D. M., & Gould, K. L. (2019). NDR Kinase Sid2 Drives Anillin-like Mid1 from the Membrane to Promote Cytokinesis and Medial Division Site Placement. *Current Biology*, *29*(6), 1055-1063.e2. https://doi.org/10.1016/j.cub.2019.01.075

Wu, J. Q., Sirotkin, V., Kovar, D. R., Lord, M., Beltzner, C. C., Kuhn, J. R., & Pollard, T. D. (2006). Assembly of the cytokinetic contractile ring from a broad band of nodes in fission yeast. *Journal of Cell Biology*, *174*(3), 391–402. https://doi.org/10.1083/jcb.200602032

Ye, Y., Lee, I. J., Runge, K. W., & Wu, J. Q. (2012). Roles of putative Rho-GEF Gef2 in division-site positioning and contractile-ring function in fission yeast cytokinesis. *Molecular Biology of the Cell*, *23*(7), 1181–1195. https://doi.org/10.1091/mbc.E11-09-0800